Applied Science and Innovative Research
ISSN 2474-4972 (Print) ISSN 2474-4980 (Online)
Vol. 9, No. 4, 2025
www.scholink.org/ojs/index.php/asir

Original Paper

An IGA-BP–Based Estimation Method for Water-Film Pressure of Marine Water-Lubricated Bearings

Donghui Li[1,2], Nan Wang[1,2], Jia Wang[1,2], Huabing Jing[1,2] & Deyang Zhao[1,2]

[1] School of Mechanical Engineering, Shaanxi University of Technology, Hanzhong 723001, China

[2] Shaanxi Key Laboratory of Industrial Automation, Hanzhong 723001, China

Received: November 5, 2025 Accepted: December 9, 2025 Online Published: December 16, 2025

doi:10.22158/asir.v9n4p98 URL: http://doi.org/10.22158/asir.v9n4p98

Abstract

Water-film pressure is a key parameter characterizing the load-carrying capacity, frictional performance, and operational stability of water-lubricated bearings; therefore, real-time and accurate monitoring is crucial to the safety of ship propulsion systems. Existing analytical, CFD, and experimental approaches are limited by operating-condition adaptability, computational burden, and cost, while conventional data-driven methods are prone to initialization sensitivity and entrapment in local optima, resulting in inadequate timeliness and accuracy. To address these issues, this study applies a back-propagation (BP) neural network to water-film pressure estimation and introduces an improved genetic algorithm (IGA) with a sine-decay mechanism to optimize the BP network's weights and biases, thereby constructing an IGA-BP model. Using rotational speed, load, and friction coefficient(COF) as inputs, the model estimates the maximum water-film pressure and its corresponding journal circular angle. Comparative evaluations on multi-condition experimental datasets show that IGA-BP attains an R^2 of 0.976; relative to BP, the root-mean-square error (RMSE) and mean absolute error (MAE) are reduced by about 53% and 79%, respectively. Compared with GA-BP, RMSE and MAE are further reduced by approximately 34% and 52%, and the model exhibits faster convergence and greater stability. Moreover, against several optimized BP variants, IGA-BP achieves the best overall metrics, offering a useful reference for research on water-lubricated bearings.

Keywords

Water-lubricated bearing, Water-film pressure estimation, BP neural network, Improved genetic algorithm

1. Introduction

In recent years, with the growing adoption of green shipping concepts, water-lubricated bearings have

become an important component of modern ship propulsion systems, owing to their environmental friendliness and low maintenance cost (Xie, Z., Jiao, J., Yang, K., et al., 2023). Under hydrodynamic lubrication, a water film forms in a water-lubricated bearing. In practical applications, the water-film pressure distribution directly affects the bearing's load-carrying capacity, frictional performance, and operational stability, and is therefore one of the key indicators for evaluating the lubrication and friction behavior of water-lubricated bearings. Moreover, the maximum water-film pressure and its corresponding journal circular angle are of great significance for optimizing bearing structural design and monitoring bearing health conditions (Ouyang, W., Liu, Q., Liang, X., et al., 2024).

Research on water-film pressure in water-lubricated bearings has mainly been conducted using theoretical analytical methods (Xie, Z., Zhang, H., Yang, M., et al., 2025), computational fluid dynamics (CFD) simulations (Li, S., Jin, Y., Luo, B., et al., 2022), and experimental testing (Liu, J., Hu, W., Sun, F., et al., 2025). Early studies primarily focused on the Reynolds equation, employing theoretical derivations to analyze the characteristics of water-film pressure in water-lubricated bearings. However, during operation, water-lubricated bearings involve low-viscosity fluids as well as complex factors such as elastic liner materials, which makes it difficult for traditional analytical models to accurately represent the actual water-film pressure behavior (Xie, Z., Jiao, J., Yang, K., et al., 2023). Although CFD can provide detailed predictions of water-film flow characteristics and pressure distribution (Mallya, R., Pai, R., & Shenoy Baloor, S., 2024), it suffers from high computational cost and poor real-time performance, and therefore cannot meet the rapid-response requirements of onboard online monitoring and intelligent control systems. Experimental testing is also expensive and time-consuming. Consequently, there is an urgent need to develop a water-film pressure estimation method that maintains high accuracy while enabling efficient and rapid response.

To characterize the strongly nonlinear mapping between multi-dimensional inputs and multi-dimensional outputs in this study, it is necessary to introduce intelligent algorithms. Problems of this kind have attracted extensive attention (Ouyang, W., Liu, Q., Liang, X., et al., 2024), and commonly used methods include artificial neural networks (ANNs) (Wang Nenzi, & Chih-Ming Tsai, 2020), k-nearest neighbors (KNN), support vector machines (SVM), and random forests (RF) (Pang Jinshan, et al., 2021). Among them, KNN and SVM are more often employed in classification and binary regression tasks; when applied to highly nonlinear multi-input multi-output (MIMO) regression, their performance is highly sensitive to the choice of the neighborhood size K, kernel type, and kernel parameters, and the coupling among hyperparameters makes tuning and generalization control difficult. RF typically entails relatively high computational complexity for such problems and requires substantial time and large sample datasets. In contrast, ANNs offer universal nonlinear approximation capability and good fault tolerance, making them well suited for strongly coupled, multi-objective regression tasks. Existing studies have applied ANNs to bearing performance evaluation and condition monitoring and have reported favorable results (Hess Nathan, & Shang Lizhi, 2022).

Among various ANN architectures, the BP neural network has gradually become an important tool for

bearing performance prediction in recent years, owing to its end-to-end modeling capability, controllable model size, low inference latency, and ease of engineering deployment (Cai, Y., Zhou, Z., & Li, Z., 2023). A BP network realizes nonlinear mapping through forward propagation and adaptively updates its weights and thresholds via backpropagation of the loss function, thereby directly supporting multi-output regression and achieving stable performance on small- to medium-sized datasets. However, BP training is highly sensitive to the initialization of weights and may become trapped in a local optimum (Chen, Z., Zhu, L., Lu, H., Chen, S., Zhu, F., Liu, S., Han, Y., & Xiong, G., 2024).

To address the limitations of BP neural networks in terms of initialization sensitivity, susceptibility to local optimum, and convergence efficiency, various metaheuristic approaches have been introduced for weight-parameter optimization. Among them, the genetic algorithm (GA) has led to the widely adopted GA-BP framework, due to its gradient-free global search capability, flexible encoding, strong adaptability to nonconvex multimodal problems, and ease of parallel implementation; its effectiveness has been demonstrated in applications such as bearing temperature prediction and vibration-signal analysis and diagnosis (Deng Changcheng, et al., 2024). However, for water-film pressure in marine water-lubricated bearings, systematic research remains limited, particularly on the joint estimation of maximum water-film pressure and the corresponding journal circular angle. This task is characterized by strong nonlinear coupling, small and noisy samples, and the periodic nature of the angle output. Under these conditions, standard GA-BP typically employs fixed crossover probability and mutation probability together with conventional fitness settings, which can readily lead to premature convergence, insufficient late-stage local exploitation, and unstable phase locking, making it difficult to balance global exploration and refined exploitation.

Therefore, this paper proposes an IGA-BP–based water-film pressure estimation method, in which an improved genetic algorithm (IGA) is employed to optimize a BP neural network. Specifically, a sine function is introduced to decay the crossover probability and mutation probability (Liu, Y., Wang, H., Ding, X., et al., 2025). In combination with mechanism-based analysis of water-lubricated bearings, the input features are refined to include rotational speed, load, and COF. The proposed model is finally validated through experiments, enabling accurate and rapid estimation of the maximum water-film pressure and its corresponding journal circular angle in marine water-lubricated bearings.

2. Water-Film Pressure Estimation Model

To accurately estimate the maximum water-film pressure of a water-lubricated bearing and its corresponding journal circular angle, this paper proposes an IGA-BP–based estimation method. The overall technical route is illustrated in Figure 1 and consists of three components:

1) Data acquisition and preprocessing. To acquire the water-film pressure inside an enclosed bearing, axial–radial through L-shaped guide holes were machined in the shaft. The holes were equally spaced in the axial and radial directions and spirally distributed at the shaft shoulder (Wang, N., Yang, L., Liang, Y., et al., 2019). Signals from the water-film pressure sensor were routed through the three front-end

holes of the guide-hole structure to a wireless monitoring node, as shown in Figure 1a. The water-film pressure was transmitted through the guide holes; the sensor was driven by constant-current excitation, and its voltage output was digitized by a data acquisition (DAQ) board and uploaded to a host computer system built around LabVIEW. The raw signals were processed using FFT filtering, which suppresses high-frequency noise while retaining the dominant spectral lines. Considering that water-film pressure contains a fundamental frequency and its harmonics, the first ten harmonics were retained, and the cutoff frequency was set to 100 Hz.

2) IGA-BP water-film pressure estimation model. A three-layer feedforward BP network was adopted as the regressor (input dimension = 3, output dimension = 2). The root mean square error (RMSE) was used as the loss function, and regularization was incorporated to mitigate overfitting. The error formulation is given in Eq. (7).

The IGA-BP estimation procedure for maximum water-film pressure is illustrated in the model-training module of Figure 1. The specific steps are as follows: (1) Bearing operating data were collected and preprocessed. To accelerate neural-network fitting and improve estimation accuracy, the monitored data were normalized and scaled to the range [0, 1]. (2) Based on correlation analysis, operating monitoring variables that exhibit strong correlation with water-film pressure were selected as input variables, while the maximum water-film pressure and the corresponding journal circular angle were taken as output variables. In the normalized dataset, the first 70% of the samples were used for training and the remaining 30% for testing. (3) A set of initial BP weights was randomly generated, and the network was trained followed by fitness evaluation, where the fitness function was defined as the root mean square error (RMSE). (4) GA parameters were set with a population size of 50, and the crossover probability and mutation probability were computed using the sine-decay mechanism. (5) New populations were generated through crossover and mutation and iteratively evaluated. The optimal solution was obtained when the RMSE of the best individual in the population converged with the average RMSE of the population. (6) The best individual was decoded to obtain the optimal initial weights, and the final IGA-BP maximum water-film pressure estimation model was trained.

3) Result presentation. The trained IGA-BP model was applied to the test operating conditions to output the maximum water-film pressure and its corresponding journal circular angle. Model accuracy and stability were evaluated using R^2, RMSE, MAE and MBE, thereby verifying the overall performance advantages of the proposed method.

2.1 BP Neural Network

A maximum-pressure estimation model for the water-lubricated bearing was developed based on a BP neural network, as shown in the model-training module of Figure 1. The training accuracy of the model is influenced by multiple parameters, among which the number of hidden-layer neurons M s the most pronounced effect. In this study, the empirical expression in Eq. (1) (Cai, Y., Zhou, Z., & Li, Z., 2023) was employed to determine the number of hidden-layer neurons.

$$M = \sqrt{R+T} + u \tag{1}$$

In Eq. (1) R is the number of inputs, T is the number of outputs, and u is a constant in the range of 1-10. Guided by the empirical expression, a grid search was conducted over the interval (Xie, Z., Zhang, H., Yang, M., et al., 2025; Liu, Y., Wang, H., Ding, X., et al., 2025) to determine the optimal number of hidden-layer neurons. The experimental results indicate that the validation error reaches its minimum when the number of hidden-layer neurons is 10, corresponding to u=8. The hyperbolic tangent function was used as the activation function in the hidden layer, and a linear function was adopted in the output layer. The learning rate was set to 0.01.

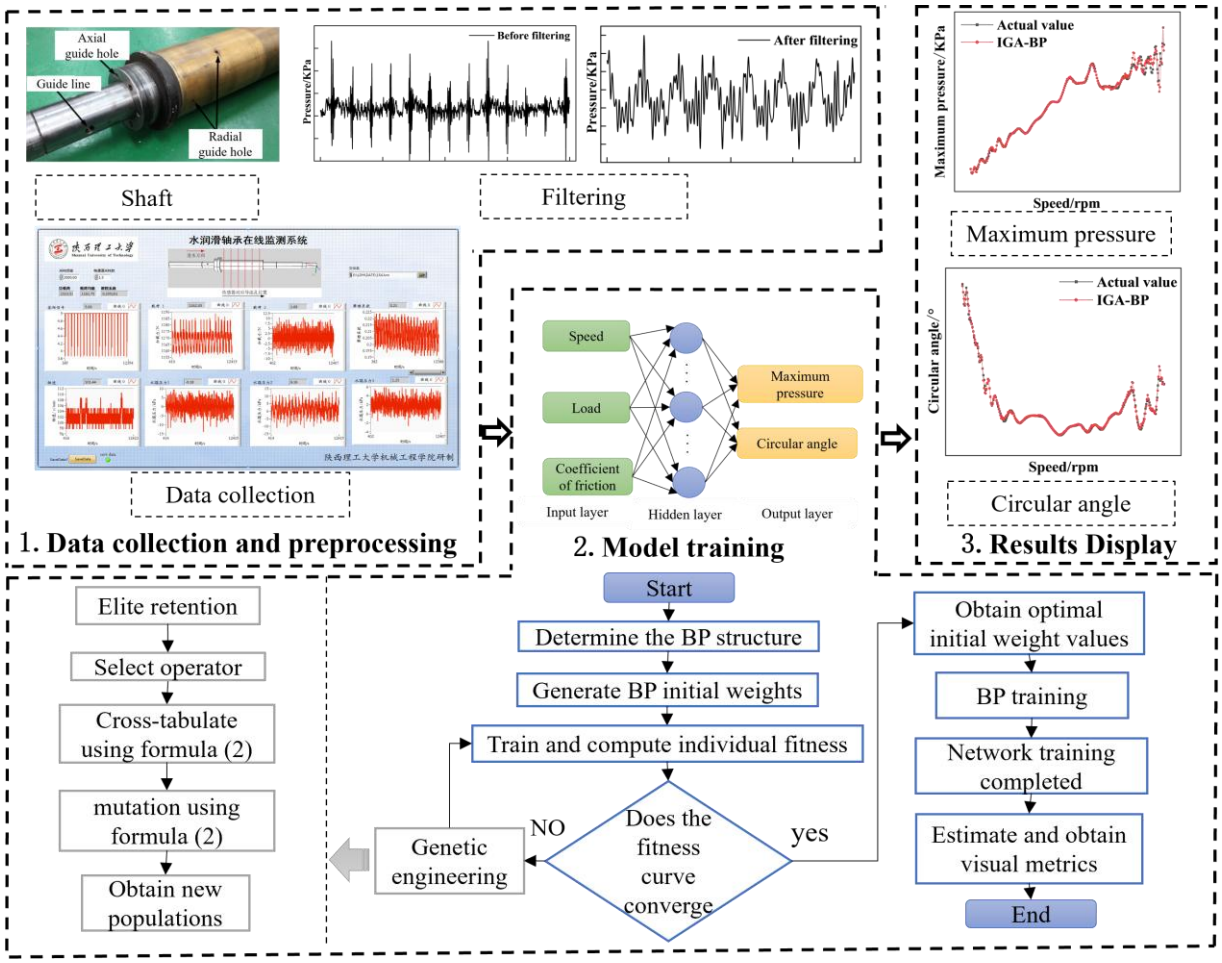

Figure 1. Estimated Model Flowchart

2.2 IGA Optimization Mechanism

In view of the task characteristics of water-film pressure estimation in water-lubricated bearings, including strong nonlinear coupling, noise disturbance, and the periodic nature of the angle output, this study introduces an IGA-BP approach with sine-decay adaptive crossover and mutation to perform global optimization of the network's weights and thresholds.

Crossover probability (P_c) and mutation probability (P_m) are key parameters that govern the algorithm's

performance. If P_c and P_m are set too low, the exploration capability becomes inadequate, population diversity decreases, and the search may be trapped in local extrema. Conversely, overly large values can disrupt the structure of high-quality individuals, thereby reducing algorithmic stability and slowing convergence. To enable dynamic parameter adjustment during evolution, a sine-decay mechanism is introduced in this study, allowing P_c and P_m to vary adaptively with the evolutionary process so as to balance global exploration and local optimization at different stages.

Specifically, in the early stage of population evolution, global search capability should be strengthened by maintaining relatively high values of P_c and P_m, so as to expand the search space, enhance population diversity, and avoid premature convergence. In the middle and late stages, as the population gradually converges toward the global optimum, P_c and P_m should be reduced to improve local search precision and refine exploration within the solution space. Accordingly, Eq. (2) is adopted in this study to control the sine decay and dynamically adjust the crossover and mutation probabilities: (Liu, Y., Wang, H., Ding, X., et al., 2025).

$$P = -\sin(\frac{t_d \pi}{2T})(P_{max} - P_{min}) + P_{max} \tag{2}$$

$$P = P_{max} - \frac{t_d}{T_{max}} \cdot (P_{max} - P_{min}) \tag{3}$$

$$P = P_{min} + (P_{max} - P_{min}) \times e^{-5 \times \frac{t}{T_{max}}} \tag{4}$$

In Eq. (2)–(4), P denotes the crossover probability and the mutation probability, t_d is the current generation index, T is the maximum number of generations, P_{max} is the upper bound of the probability, and P_{min} is the lower bound of the probability.

To clearly examine how the crossover probability and mutation probability evolve, the maximum number of generations was set to T=50, with the ranges of the crossover and mutation probabilities specified as [0.4,0.99] and [0.001,0.1], respectively. As shown in Figure 2, a sine function over the interval [0,π/2] was adopted to impose sine-decay behavior on both probabilities. Compared with fixed-parameter settings, this strategy adaptively regulates the behavior of genetic operators, thereby improving algorithmic stability and optimization capability.

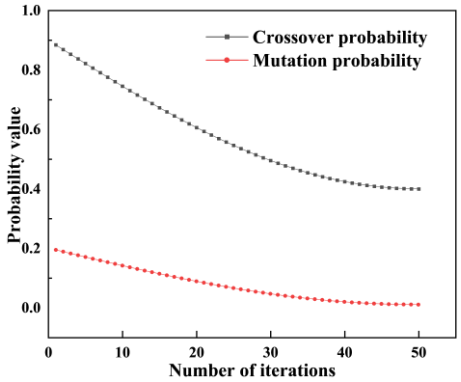

Figure 2. Crossover Mutation Probability Curves

To verify the superiority of the proposed sine-decay mechanism in optimizing the water-film pressure estimation model for water-lubricated bearings, performance was evaluated—under the same population size—against three mainstream decay strategies: linear decay, exponential decay, and fixed probability. The linear- and exponential-decay formulations are given in Eqs. (3) and (4), respectively. For the fixed-probability strategy, the conventional genetic algorithm settings were adopted, with the crossover probability set to 0.7 and the mutation probability set to 0.05. As shown in Figure 3, the sine-based improved strategy more effectively balances global search and local exploitation, thereby avoiding premature convergence and achieving higher solution accuracy than the traditional strategies.

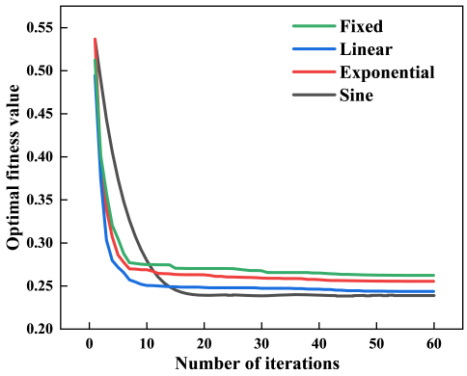

Figure 3. Comparison of Decay Strategies

The sine-decay adaptive crossover and mutation probability mechanism enables a dynamic balance between exploration capability and convergence capability throughout the evolutionary process of the genetic algorithm. This improves the algorithm's adaptability to complex search spaces, strengthens both its global optimization capability and its local exploitation capability, and consequently yields superior estimation performance and training efficiency when optimizing the BP neural network.

3. Experimental System and Data Description

Considering the operating environment and working conditions of a marine stern bearing, an acquisition

system was designed using rotational speed, load, COF, and water-film pressure as experimental measurement parameters. The mapping relationship between water-film pressure and shaft rotational speed, load, and COF can be fitted using machine learning algorithms.

3.1 Water-Lubricated Bearing Test Bench

The online monitoring test bench for water-lubricated bearings is shown in Figure 4. It consists of a three-phase asynchronous motor, a speed–torque sensor, a hydraulic loading device, pressure sensors, a wireless monitoring node, and a host computer. The three-phase induction motor serves as the power source of the test bench. Loads are applied to the bearing under different operating conditions using the hydraulic loading devices on both sides of the bearing. The monitoring node is installed on the overhung side of the shaft and is responsible for acquiring and transmitting key operating parameters during bearing operation. The test bearing is a water-lubricated bearing made of PEEK (polyether ether ketone), with a length-to-diameter ratio of 1.2 and an inner diameter of 100 mm. The lubrication system supplies water to the bearing at a pressure of 0.1 MPa; the inlet and outlet ports are located on the left and right end covers, respectively.

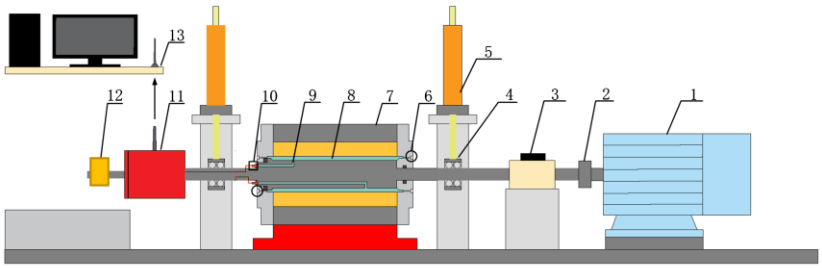

1. 3-phase asynchronous motor; 2. Coupler; 3. Speed and torque sensors; 4. Rolling bearing;
5. Hydraulic loading device; 6. Water system; 7. Water lubrication bearing; 8.Water film;
9.Deflector hole; 10. Pressure transducer; 11. Monitoring node;
12. Conductive slip ring; 13. Host computer

Figure 4. Water-lubricated Bearing Test Bench

3.2 Test Plan

To replicate operating conditions of a marine stern bearing, medium-to-high-speed tests with adjustable load were designed, with the load regulated in closed loop by a bidirectional hydraulic loading system. Considering the hydrostatic pressure at a water depth of approximately 10 m (≈0.1 MPa), the baseline water supply pressure was set to 0.1 MPa, and it was increased to 0.4 MPa during the running-in stage to stabilize the surface condition of the tribo-pair. The sampling frequency of the data acquisition card was 2000 Hz. The tests included three categories of operating conditions:

(1) Running-in: a moderate load and a relatively high water supply pressure were applied to stabilize the journal–bush surface condition.

(2) Speed variation: the rotational speed was increased in steps under a fixed load to investigate the response of the pressure amplitude and the peak-angle position to speed.

(3) Load variation: the load was adjusted in stages at representative rotational speeds to evaluate the

influence of load changes on the water-film pressure distribution and peak shift.

After the running-in stage, data were collected over an operating-condition matrix with rotational speeds ranging from 100 to 400 rpm and unit bearing pressures of 0.10, 0.15, 0.20, and 0.25 MPa, corresponding to 1200, 1800, 2400, and 3000 N, respectively. For each condition, measurements were recorded after the system reached a steady state. After completion of the tests, the rig was shut down and the water supply was turned off.

3.3 Data Description

The continuous signals acquired during the tests were segmented into individual revolutions using a phase reference signal, and the water-film pressure over one period at a bearing cross-section was selected. Because the applied load is mainly supported by the lower half of the bearing, only the water-film pressure corresponding to the lower half was processed. As shown in Figure 5, one sampling point was taken every 2° along the lower-half circumference, yielding a total of 91 points; point P_1 was set at 0°, and the points were counted counterclockwise. From the processed pressure data, the maximum water-film pressure and its corresponding journal circular angle were extracted as the model outputs.

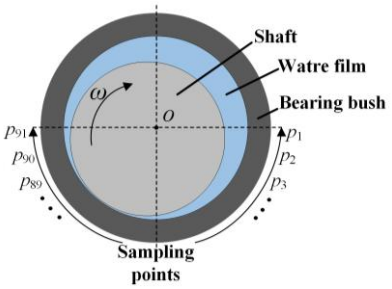

Figure 5. Sampling Point Diagram

According to the theory of hydrodynamic lubrication, the water-film pressure distribution in a water-lubricated bearing is governed by the Reynolds equation. In practical manufacturing, neither the surface of the bearing bush nor that of the journal can be perfectly smooth, and random micro-asperity contact exists between the two surfaces. The modified average Reynolds equation is given in Eq. (5) (Xie, Z., Zhang, H., Yang, M., et al., 2025):

$$\frac{\partial}{\partial x}\left(\phi_x g h^3 \frac{\partial p}{\partial x}\right)+\frac{\partial}{\partial z}\left(\phi_z g h^3 \frac{\partial p}{\partial z}\right)=6\eta u g \frac{\partial}{\partial x}\left(h+\sigma_s \phi_s\right) \tag{5}$$

In Eq. (5), x and z are the circumferential and axial coordinates, respectively, on the unwrapped bearing surface; u is the relative speed between the shaft and the bearing; g is the film fill ratio; h is the water-film thickness; σ_s is the composite surface roughness; p is the water-film pressure in the bearing; η is the dynamic viscosity of water; ϕ_x and ϕ_z are the pressure flow factors in the x and z directions, respectively; ϕ_s is the shear flow factor; and $V_1$and V_2 are the tangential surface velocities of the journal and the bearing bush, respectively.

Rotational speed is the primary driving factor for hydrodynamic effects and is positively correlated with

pressure. The macroscopic load governs the microscopic distribution of water-film thickness: as the load increases, the eccentricity ratio increases, the minimum water-film thickness decreases, and the peak pressure rises. The COF represents the combined effects of fluid shear and load, reflects the lubrication regime (hydrodynamic/mixed/boundary lubrication), and is highly sensitive to nonlinear variations in the pressure field.

The Pearson correlation coefficient *r* was used to quantify the influence of each factor on the maximum water-film pressure and its angular location, and factors with high correlation were selected as model inputs. The Pearson correlation coefficient *r* is given in Eq. (6). Using Pearson correlation analysis, the correlation coefficients between the bearing operating parameters and the maximum water-film pressure as well as its corresponding journal circular angle were calculated, and the results are listed in Table 1. The rotational speed exhibits an extremely strong correlation, whereas the load and COF show strong correlations.

$$r = \frac{\sum_{i=1}^{n}(a_i - \bar{a})\left(b_i - \bar{b}\right)}{\sqrt{\sum_{i=1}^{n}(a_i - \bar{a})^2}\sqrt{\sum_{i=1}^{n}\left(b_i - \bar{b}\right)^2}} \tag{6}$$

In Eq. (6), a_i and b_i are the values of the model input and output variables, respectively; $\bar{a}$ and $\bar{b}$ are the mean values of the two variable sets; and n is the number of samples.

Table 1. Correlation Coefficient

Influencing factor	Maximum water-film pressure	Journal circular angle
Speed	0.93	-0.85
Load	-0.77	-0.50
COF	-0.87	0.79

The test system provided circumferential pressure measurements under different operating conditions. Since the model inputs should reflect the bearing operating state, rotational speed, load, and the COF were selected as input features based on physical mechanisms and Pearson correlation analysis, and this selection has clear physical significance.

Figure 6 presents the data of the maximum pressure and its corresponding journal circular angle under four different load conditions. It can be observed that the maximum pressure increases with increasing speed and shows an overall increase as the load becomes larger. In addition, the journal circular angle associated with the maximum pressure tends to become more stable as the speed increases.

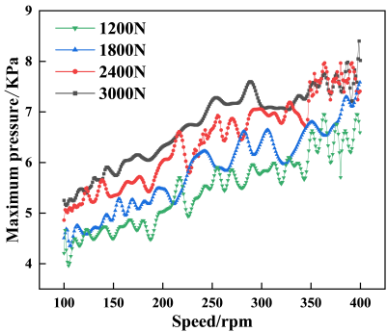

(a) Maximum pressure

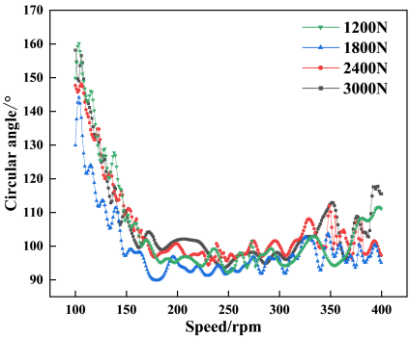

(b) Journal circular angle

Figure 6. Data Visualization of Maximum Pressure and Journal Circular Angle

4. Results and Analysis

4.1 Results and Analysis

Four evaluation metrics—coefficient of determination R^2, root mean square error (RMSE), mean absolute error (MAE), and mean bias error (MBE)—were used to comprehensively assess model performance. A value of R^2 closer to 1 indicates stronger explanatory power. RMSE characterizes the standard-deviation scale of the error and is more sensitive to large deviations (smaller is better). MAE reflects the typical absolute deviation and is more robust to outliers (smaller is better). MBE is the signed mean error and is used to examine systematic bias (a value closer to 0 is preferred). The metrics are calculated as shown in Eq. (7).

$$R^2 = 1 - \frac{\sum_{i=1}^{m}(\hat{y}_i - y_i)^2}{\sum_{i=1}^{m}(\bar{y}_i - y_i)^2}$$

$$RMSE = \sqrt{\frac{1}{m}\sum_{i=1}^{m}(y_i - \hat{y}_i)^2} \quad (7)$$

$$MAE = \frac{1}{m}\sum_{i=1}^{m}|y_i - \hat{y}_i|$$

$$MBE = \frac{1}{m}\sum_{i=1}^{m}(y_i - \hat{y}_i)$$

In Eq. (7), y_i is the true value of the model output, $\hat{y}_i$ is the estimated value of the model output, $\bar{y}_i$ is the mean of the true output values, and m is the number of samples.

4.2 Comparison of Different Algorithms

4.2.1 Assessment of Improvement Effectiveness

As shown in Figure 7, the estimation curve of maximum water-film pressure obtained by IGA-BP nearly overlaps with the measured curve across the entire range of operating conditions. The peaks and turning points are well aligned, with no systematic phase lag or lead. In addition, the attenuation of amplitudes at local sharp spikes is effectively suppressed, indicating that the model captures the detailed pressure pulsations while maintaining a stable fit to the overall trend.

Using the same dataset, BP, GA-BP, and IGA-BP were compared, and estimation validation was carried out on the collected samples. The comparison results are shown in Figure 8. All three models are able to reproduce the overall long-term upward trend along the sample sequence, indicating that the underlying nonlinear mapping has been learned. BP and GA-BP provide accurate estimation at the large-scale trend level, capturing the overall profile of the ground truth with no pronounced long-term bias. The differences mainly arise in local details and high-frequency fluctuations in the middle-to-late portion of the sequence. BP exhibits noticeable phase lag and amplitude compression at multiple peaks, valleys, and minor downturn segments; turning points are often over-smoothed, showing a tendency to "follow the main trend while losing details." GA-BP improves the tracking of turning points and peaks; however, slight lag and amplitude underestimation persist in highly fluctuating regions, where local sharp spikes are prone to being smoothed out. While maintaining comparable global trend-fitting capability to BP and GA-BP, IGA-BP shows better performance in capturing fine-scale variations.

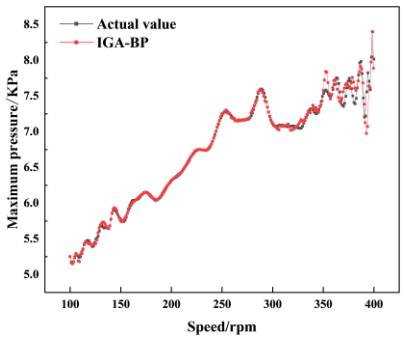

(a) Maximum pressure estimation

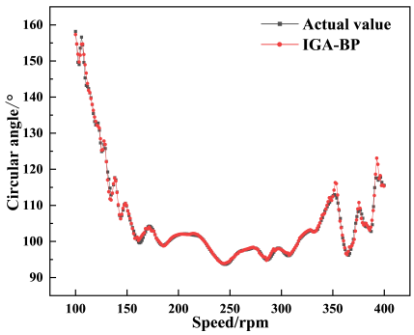

(b) Journal circular angle estimation

Figure 7. IGA-BP Model Estimation Curve

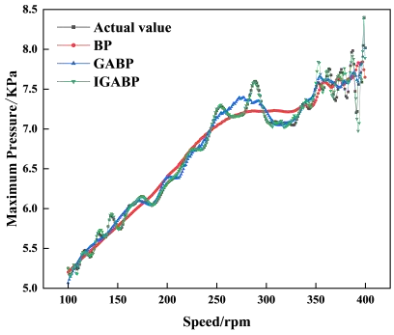

(a) Maximum pressure estimation

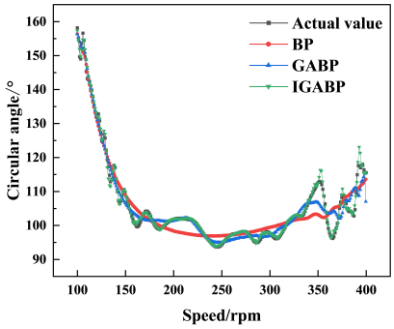

(b) Journal circular angle estimation

Figure 8. Comparison of Model Estimation Curves

Under 20 repeated experiments, the mean values of the evaluation metrics were used for comparison. Figure 9 shows the average performance of the BP, GA-BP, and IGA-BP models in estimating the maximum water-film pressure. The BP model achieves an R^2 of only 0.893, with relatively large prediction errors (RMSE = 4.581, MAE = 3.525), indicating clear limitations in fitting complex nonlinear mappings. After introducing the genetic algorithm, the overall performance of the GA-BP model improves, with R^2 increasing to 0.947 and RMSE and MAE decreasing to 3.132 and 2.035, respectively, confirming the effectiveness of global optimization in improving prediction accuracy. In contrast, the proposed IGA-BP model delivers the best results across all metrics: R^2 reaches 0.976, while RMSE and MAE decrease to 2.195 and 0.975. Compared with the BP model, RMSE and MAE are reduced by

approximately 52% and 72%, respectively, demonstrating the high accuracy of IGA-BP for pressure estimation.

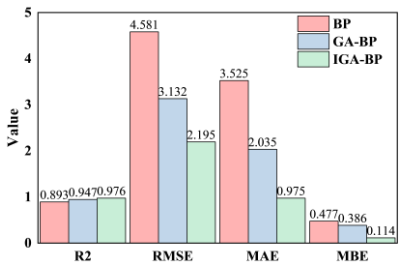

Figure 9. Comparison of Model Metrics for Different Algorithms

4.2.2 Comparison of Multiple Optimization Algorithms

To further verify the robustness and performance of the improved genetic algorithm, comparisons were conducted against several classical optimization algorithms.

Because the training and test sets are randomly selected, the evaluation metrics for each method should be reported as the average over multiple repeated experiments.

Table 2. Validation Results of Different Optimization Models

	R^2	RMSE	MAE	MBE
DBO-BP	0.927	3.947	2.265	0.250
SAO-BP	0.959	2.945	2.226	0.394
SA-BP	0.960	2.866	2.223	0.361
WOA-BP	0.947	3.048	2.231	0.460
GWO-BP	0.953	3.114	2.375	0.392
IGA-BP	0.976	2.195	0.975	0.114

The models were trained 20 times and the results were averaged, as summarized in Table 2. The optimization algorithms were compared using four metrics (R^2, RMSE, MAE, and MBE). The IGA-BP model achieves the highest R^2, indicating the best goodness of fit, while yielding the lowest values across the three error metrics, suggesting the smallest systematic bias and the best overall performance. These results demonstrate that IGA-BP outperforms the other optimization algorithms in both accuracy and stability.

4.2.3 Generalization Ability Analysis

To assess the model's generalization ability, estimation comparisons were conducted on four datasets obtained under different load conditions. As shown in Figure 10, when the four load cases are considered together, the radar plot of IGA-BP exhibits a noticeably higher vertex along the R^2 axis, while extending

less along the RMSE, MAE, and MBE axes, resulting in a profile closest to the ideal diamond shape. Meanwhile, as the load varies from 1200 N to 3000 N, the polygon's shape and area remain stable, indicating that the model also shows strong generalization performance across operating conditions.

Without relying on any specific load condition, IGA-BP demonstrates an overall advantage in explainability, accuracy, and unbiasedness, and shows the smallest variation across different loads, confirming its stability in estimating the maximum water-film pressure.

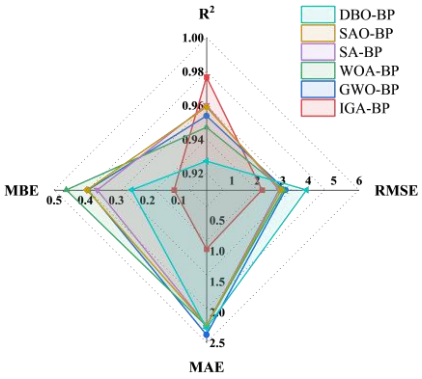

(a) Load 1200N

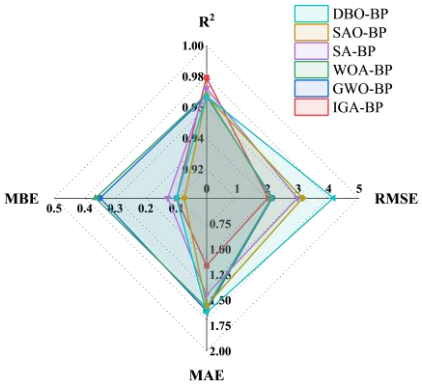

(b) Load 1800N

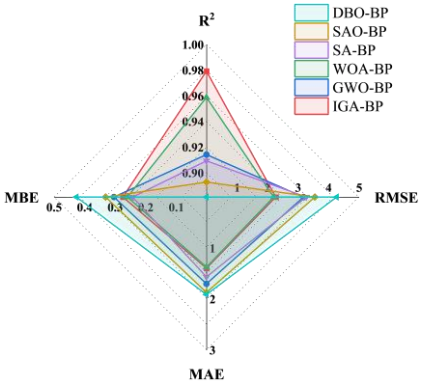

(c) Load 2400N

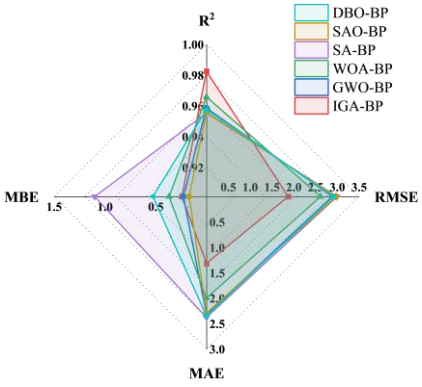

(d) Load 3000N

Figure 10. Model Comparison across Different Datasets

5. Conclusion

Focusing on a water-film pressure estimation method for water-lubricated bearings, this study establishes an IGA-BP model with rotational speed, load, and friction coefficient (COF) as inputs, and maximum water-film pressure and its corresponding journal circular angle as outputs. By introducing sine decay to the genetic algorithm's crossover probability and mutation probability, the proposed approach coordinates global exploration in the early evolutionary stage with local refinement in the later stage. This effectively alleviates BP initialization sensitivity as well as GA premature convergence and local optimum issues, while reducing the loss of fine-scale details. The main conclusions are as follows:

(1) Experimental validation using measured data shows that the proposed model exhibits a high degree of agreement with the ground-truth curves in terms of both overall trend and local fluctuations. Compared with the BP model, RMSE and MAE are reduced by approximately 52% and 72%, respectively, and stable, non-saturating behavior is maintained even in the high-speed range. In addition, peaks, valleys, and turning points in the angle corresponding to the maximum pressure are accurately captured.

(2) Comparisons with GWO-BP, WOA-BP, SA-BP, SAO-BP, and DBO-BP show that the proposed model achieves the best overall performance across all four metrics. Specifically, RMSE is generally reduced by 24%–27%, and MAE is reduced by 66%–67%, demonstrating superior accuracy and robustness.

References

Cai, Y., Zhou, Z., & Li, Z. (2023). Optimization Study of BP Neural Network Based on Genetic Algorithm. *2023 IEEE International Conference on Electrical, Automation and Computer Engineering* (ICEACE), *2023*, 1555-1560. https://doi.org/10.1109/ICEACE60673.2023.10442575

Chen, Z., Zhu, L., Lu, H., Chen, S., Zhu, F., Liu, S., Han, Y., & Xiong, G. (2024). Research on bearing fault diagnosis based on improved genetic algorithm and BP neural network. *Scientific Reports*, *14*(1), 15527. https://doi.org/10.1038/s41598-024-66318-0

Deng Changcheng, et al. (2024). A friction temperature model for dynamic bearing operation based on neural network and genetic algorithm. *Tribology International*, *191*(2024), 109057.

https://doi.org/10.1016/j.triboint.2023.109057

Hess Nathan, & Shang Lizhi. (2022). Development of a machine learning model for elastohydrodynamic pressure prediction in journal bearings. *Journal of Tribology*, *144*(8), 081603. https://doi.org/10.1115/1.4053815

Li, S., Jin, Y., Luo, B., et al. (2022). Research on liquid film modeling method of water lubricated bearing considering shaft bending. *Ship Science and Technology*, *44*(21), 36-40.

Liu, J., Hu, W., Sun, F., et al. (2025). Tribological Properties of SF-2A Materials Water-lubricated Stern Bearings with Different Flume Distributions. *Lubrication Engineering*, *50*(05), 20-27.

Liu, Y., Wang, H., Ding, X., et al. (2025). Optimization of nutrient solution temperature prediction model of LSTM based on improved genetic algorithm. *Journal of Chinese Agricultural Mechanization*, *46*(06), 91-97.

Mallya, R., Pai, R., & Shenoy Baloor, S. (2024). Nonlinear transient analysis of water lubricated bearing in the turbulent regime. *Scientific Reports*, *14*(1), 26871. https://doi.org/10.1038/s41598-024-78242-4

Ouyang, W., Liu, Q., Liang, X., et al. (2024). Data-driven model of the distribution lubrication on water-lubricated bearing under severe operating conditions. *Journal of Tribology*, *146*(1). https://doi.org/10.1115/1.4062900

Pang Jinshan, et al. (2021). Classification of friction and wear state of wind turbine gearboxes using decision tree and random forest algorithms. *Journal of Tribology*, *143*(9), 091702. https://doi.org/10.1115/1.4049257

Wang Nenzi, & Chih-Ming Tsai. (2020). Assessment of artificial neural network for thermohydrodynamic lubrication analysis. *Industrial Lubrication and Tribology*, *72*(10), 1233-1238. https://doi.org/10.1108/ILT-03-2020-0109

Wang, N., Yang, L., Liang, Y., et al. (2019). Non-contact Electromagnetic Loading Monitoring System for Water-lubricated Bearings. *China Mechanical Engineering*, *30*(24), 3004-3009.

Xie, Z., Jiao, J., Yang, K., et al. (2023). A state-of-art review on the water-lubricated bearing. *Tribology International*, *180*, 108276. https://doi.org/10.1016/j.triboint.2023.108276

Xie, Z., Zhang, H., Yang, M., et al. (2025). Research on the Influence of Bidirectional Misalignment on the Lubrication Characteristics of Water-Lubricated Grooved Bearings. *Tribology*, *45*(11), 1706-1717.